

# Correlating the Sodium Storage Mechanism and Enhancing the Initial Coulombic Efficiency of Biomass-Derived Hard Carbon in Sodium-Ion Batteries

Rajib Samanta, Suryakanta Senapati, Maripi Kala, and Sudip Barman\*

Traditional graphite-based anode materials perform poorly in sodium-ion battery (SIB) due to their insufficient interlayer spacing. Hard carbon has received much attention as anode material for SIBs. Biomass materials are a perfect source of hard carbon precursors due to their inherent benefits and ability to be renewed. Herein, silicon/hard carbon (Si/HC-X) composite is synthesized from *Citrus limon* leaves as a useful anode material for SIBs. The intrinsic doping of silicon in carbon matrixes increases interlayer distance as well as defects, which promotes mass transportability and  $\text{Na}^+$  adsorption capacity. The optimized Si/HC-1100 electrode shows  $\approx 261 \text{ mAh g}^{-1}$  of reversible specific capacity with  $\approx 79.8\%$  initial Coulombic efficiency (ICE). Additionally, the composite exhibits  $\approx 87.4\%$  capacity retention

at  $200 \text{ mA g}^{-1}$  after 200 cycles. The plateau capacity increases from Si/HC-900 to Si/HC-1300 as the micro- and nanopores formation increases with increasing calcination temperature. The expanded-interlayer distance contributes to the plateau capacities, whereas slope capacity arises due to adsorption of  $\text{Na}^+$  on defects and open pores. The galvanostatic intermittent titration technique, ex-situ XRD and Raman analysis suggest “adsorption-intercalation-pore filling” mechanism, where intercalation contributes more to the plateau capacity of Si/HC-1100. Moreover, the full-cell ( $\text{Si/HC-1100}||\text{Na}_3\text{V}_2(\text{PO}_4)_3$ ) achieves a maximum  $207 \text{ mAh g}^{-1}$  reversible capacity from the anode side and remarkable cycle stability.

## 1. Introduction

The lithium-ion batteries (LIBs) have emerged as the state-of-the-art devices for more than three decades as of now.<sup>[1]</sup> In spite of the growing call for LIBs, lithium and other transition metals are a prime subject due to their low abundance and uneven distribution in the Earth's crust.<sup>[2]</sup> To tackle this adversity, researchers around the globe have shifted to sodium-ion batteries as a renewable energy device that exhibits similar chemical and physical properties as lithium, having the advantages of low cost, fair abundance, and wide distribution in the Earth's crust of sodium resources.<sup>[3,4]</sup> The selection of materials for the perfected anode and cathode is crucial for the optimization of SIBs for practical applications. Fortunately, various materials for cathode, including layered oxides,<sup>[5,6]</sup> polyanionic compounds,<sup>[7,8]</sup> and Prussian blue

analogs,<sup>[9,10]</sup> have emerged as potentially robust in the practical applications of sodium-ion batteries with enhanced safety fair energy density, and commendable cycling stability. In spite of the noteworthy advances in cathode materials, an open quest still persists to achieve the perfect coupling anode for SIBs.<sup>[11]</sup> The optimized anode materials for LIBs cannot be substituted for SIBs, owing to the fact that the larger ionic radius of sodium ions hinders the kinetics of sodiation/desodiation, in contrast to the feasible interaction of the small  $\text{Li}^+$  ions with the material.<sup>[12,13]</sup> Therefore, integration of the typical commercialized graphite anode (for LIBs) in SIBs presents a hurdle to the insertion and deintercalation process of sodium ions, resulting in compromised energy storage capacity.<sup>[14–17]</sup> Thus, the current major challenge in optimizing battery reliability and developing sustainable sodium battery systems lies in developing the most suitable materials for anode applications.

Research endeavors hitherto have established “Hard Carbon” as the most efficient anode material for sodium-ion batteries as a consequence of its superior electrochemical performance.<sup>[18,19]</sup> The features attributing to the supremacy of hard carbons (HCs) as anode material for SIBs are the widespread micropores and large interlayer spacing in the carbon fringes, resulting in a high storage capacity of  $\approx 300 \text{ mAh g}^{-1}$  and low operation voltage.<sup>[20,21]</sup> Moreover, the hard carbon anode also displays an exceptionally low voltage plateau at 0.1 V, along with a high specific capacity, low redox potential, and high energy density.<sup>[22,23]</sup> To add up the benefits of sustainability, broad production source, large yield, low cost, and upholding the principles of green chemistry, biomass as the parent origin of hard carbons has been extensively studied and worked on.<sup>[24]</sup> Biomass largely comprises

R. Samanta, S. Senapati, M. Kala, S. Barman

School of Chemical Sciences

National Institute of Science Education and Research (NISER)

HBNI

Bhubaneswar, Orissa 752050, India

E-mail: sbarman@niser.ac.in

R. Samanta, S. Senapati, M. Kala, S. Barman

Homi Bhabha National Institute

Training School Complex

Anushaktinagar, Mumbai 400094, India

 Supporting information for this article is available on the WWW under <https://doi.org/10.1002/batt.202500295>

 © 2025 The Author(s). *Batteries & Supercaps* published by Wiley-VCH GmbH. This is an open access article under the terms of the Creative Commons Attribution License, which permits use, distribution and reproduction in any medium, provided the original work is properly cited.

carbon and plant nutrients, along with a rich porous structure, large specific surface area, and more oxygen-containing active groups on the surface.<sup>[25]</sup> Numerous biomass sources such as pine nutshell,<sup>[26]</sup> orange peel,<sup>[27]</sup> grass,<sup>[28]</sup> tea,<sup>[29]</sup> rape shell,<sup>[30]</sup> peanut shell,<sup>[31]</sup> banana peel,<sup>[32]</sup> nutshell,<sup>[33]</sup> pine nut,<sup>[34]</sup> grapefruit peel,<sup>[35]</sup> pistachio shell,<sup>[36]</sup> rice husk,<sup>[37]</sup> and leaves<sup>[38]</sup> have been broadly reported as hard carbon precursors. "Citrus limon" leaves are an abundant agricultural by-product in nations that cultivate lemon.<sup>[39]</sup> The "Citrus limon" leaves possess a good amount of silica, which can be used as cost-effective resources for Si material fabrication. The presence of Si in carbon matrix is a good candidate for LIBs, because Li possesses alloying reaction with Si.<sup>[40]</sup> On the other hand, Si-based materials are still unexplored for SIBs. Even though Si is electrochemically active in sodiation and NaSi and NaSi<sub>2</sub> phases have been confirmed to exist, no reports about Si and Na electrochemical reaction have been documented, because the alloying reaction of Na with Si is less favorable and possesses low capacity.<sup>[41]</sup> However, atomic distribution of Si into hard carbon can increase the interlayer distance of the pseudo-graphitic layer of the hard carbon, thereby increasing the plateau capacity.<sup>[42]</sup> Therefore, "Citrus limon" can be a good candidate for the synthesis of industrial hard carbon for SIB anodes.

The arrangement of carbon layers in HCs is random, which poses complexity in its structure, creating many conflicts as on the claims of sodium storage mechanisms in HCs. In 2000, Stevens et al.<sup>[43,44]</sup> first proposed the "insertion-filling" mechanism to explain the mechanistic response of sodium ions in HCs derived from glucose. Conversely, an "adsorption-filling" mechanism was revealed in recent investigations, which suggests that capacity above 0.1 V is due to defect adsorption, whereas capacity below 0.1 V is due to nanopores filling.<sup>[45–47]</sup> Other reports have found the "adsorption-insertion" mechanism further complicating the idea of sodium storage in HCs.<sup>[46,48,49]</sup> Presently, some researchers also show the "adsorption-insertion-filling" mechanism for Na<sup>+</sup> storage in HCs.<sup>[50–52]</sup> It has furthermore been advocated that the sodium storage in HCs, apart from the "adsorption-insertion-filling" mechanism, also includes the formation of sodium clusters.<sup>[53]</sup> However, it is unclear how biomass-derived inherent Si-doped HCs affect the sodium storage mechanism. Therefore, more research is required to solve the ambiguity of the Na<sup>+</sup> storage mechanism in hard carbons.

In this study, silicon hard carbon (Si/HC-X) composites were synthesized for SIBs from *Citrus limon* (lemon) leaves by

high-temperature thermal treatment in an argon atmosphere. The inherent Si doping increases the interlayer spacing of carbon, which facilitates charge and mass transfer kinetics. An optimized specific capacity of ≈261 mAh g<sup>-1</sup> was found for Si/HC-1100 at 25 mA g<sup>-1</sup> current density with ≈79.8% ICE. It is also found that the Si/HC-1100 exhibits a reversible capacity of 84.6 mAh g<sup>-1</sup> with 87.4% retention after 200 cycles at a current density of 200 mA g<sup>-1</sup>. The galvanostatic intermittent titration technique (GITT) study shows a high Na<sup>+</sup> diffusion rate in the Si/HC-1100 electrode. Additionally, the full-cell (Si/HC-1100 || NVP) also exhibits excellent cycling stability and a high capacity of ≈207 mA h g<sup>-1</sup> from the anode side at 25 mA g<sup>-1</sup> current density.

## 2. Experimental Section

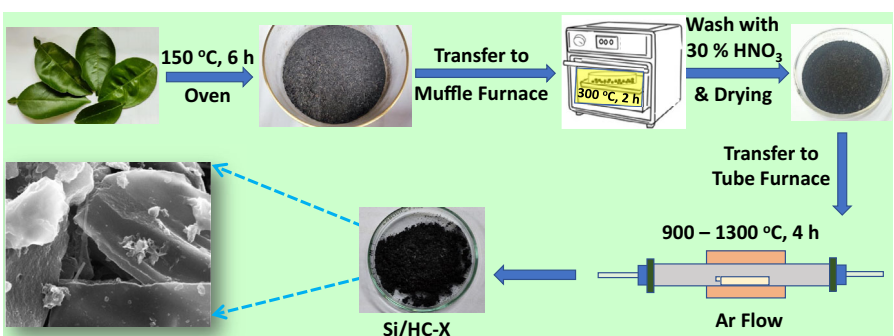
### 2.1. Materials and Chemicals

*Citrus limon* (lemon) leaves (source for Si and HC) used in this study were obtained from the National Institute of Science Education and Research (NISER), India. Na metal, sodium hexafluorophosphate (NaPF<sub>6</sub>), ethylene carbonate (EC), diethyl carbonate (DEC), and dimethyl carbonate (DMC) were purchased from Sigma-Aldrich. PVDF Binder (MTI), carbon black (Super-P, MTI), and Na<sub>3</sub>V<sub>4</sub>(PO<sub>4</sub>)<sub>3</sub> (NVP) (MTI) were used for the synthesis and electrochemical study of the electrodes. Glass microfiber (GF/D) separator was bought from Merck. All of these chemicals were used without further purification. Mili-Q water was collected from a Mili-Q (Millipore) ultra-filtration system with 35 mho/cm conductivity at 25 °C.

### 2.2. Synthesis of Silicon Hard Carbon Composites (Si/HC-X)

A schematic presentation for the synthesis of Si/HC-X is shown in Scheme 1.

About 200 g of lemon leaves were hand-picked and transformed into silicon hard carbon composites (Si/HC). The leaves were first heated at 150 °C for 6 h in a hot air oven, followed by heating at 300 °C in a muffle furnace at a ramping rate of 5 °C min<sup>-1</sup> for 2 h. Then, the obtained crude carbon precursor was kept in 30% HNO<sub>3</sub> solution overnight to dissolve any inorganic impurities if present. The carbon suspended in inorganic acid was washed several times over with deionized water. The powder X-ray



Scheme 1. Schematic representation for the synthesis of Si/HC-X.

diffraction study was carried out to monitor whether the impurities were removed. After washing, only silicon was present in the carbon matrix. The carbon residue was then dried at 80 °C overnight. It was then thermally treated at various temperatures in an argon (Ar) atmosphere in a tube furnace at 5 °C min<sup>-1</sup> ramping rate for 4 h to transform it into silicon-containing hard carbon (Si/HC-X). Depending on the different heating temperatures, the products were named Si/HC-X, where X is the heating temperature, such as Si/HC-900, Si/HC-1100, and Si/HC-1300, respectively.

We also synthesized Si/HC-1100 (porous) and HC-1100 composites to know the effect of synthesis strategy and Si-dopant in the composite. The Si/HC-1100 (porous) compound was synthesized in a similar method by removing the impurities after the calcination, while HC-1100 was synthesized by removing the Si by HF etching for overnight in a Teflon pot having 20% HF on it followed by calcination at 1100 °C temperature.

### 2.3. Electrochemical Measurements

#### 2.3.1. Half-Cell

For electrochemical measurements, half-cells with Si/HC-X anodes were prepared by mixing the active material (Si/HC-X), conductive carbon (Super P), and PVDF binder in the ratio of 9:0.5:0.5 by mass. The slurry of the above was made using appropriate NMP solvent ( $\approx$ 0.15 mL). Then, the slurry was applied evenly on a carbon-coated aluminum (Al) current collector. The slurry was applied to the current collector by the continuous process of drying the film at 80 °C. The coated collector was stored in a vacuum oven at 110 °C overnight to remove any moisture or excessive solvent that may have persisted on the coated material. The coated material was then hot pressed and punched into a disk of 15 mm diameter using a manual punching machine. The material loading weight of the electrodes was found to be between 1.5–3.5 mg. Coin cells in cell case CR2032 were assembled in an Ar-filled glove box with O<sub>2</sub> and H<sub>2</sub>O levels lower than 0.1 ppm using the Whatman GF/C 1822-047 separator and pure sodium metal as a counter electrode. The electrolyte used was a

solution of NaPF<sub>6</sub> (1 M) in a 2:1:1 volumetric mixture of ethylene carbonate (EC), dimethyl carbonate (DMC), and diethyl carbonate (DEC). The charge–discharge performance study was conducted in an Arbin Instruments battery cycler in the potential range of 0.01–2.5 V (Na/Na<sup>+</sup>) at various charge densities. Cyclic voltammetry (CV) was performed in the same potential range with different scan rates with Pine potentiostat. Electrochemical impedance spectroscopy (EIS) experiments to obtain Nyquist plots were performed in the frequency range of 100 kHz to 0.01 Hz using an electrochemical Autolab workstation. GITT measurements were carried out in a Corrtest electrochemical workstation.

#### 2.3.2. Full-Cells

The full cells were also assembled in a CR2032 case coin cell exactly as stated above for the half cells inside an Ar-filled glove box with O<sub>2</sub> and H<sub>2</sub>O levels below 0.1 ppm. The anode electrode was prepared as stated above, while for cathode electrode preparation, a slurry of NVP, conductive carbon (super P), and PVDF binder in the ratio of 8:1:1 in NMP was coated on Al current collector by the same procedure as stated above.

## 3. Results and Discussions

### 3.1. Materials Characterization

At first, the structure and morphology of the compounds were examined using field emission-scanning electron microscopy (FE-SEM) and transmission electron microscopy (TEM). The FESEM images of carbonized leaves and carbonized leaves after acid wash are shown in Figure S1a,b, Supporting Information, respectively. Both images show sheet-like morphology. The surface of Figure S1b, Supporting Information, image shows little exfoliation of the surface which could be due to the acid wash and disintegration of impurities during the process. FESEM images of Si/HC-900, Si/HC-1100, and Si/HC-1300 are also shown in Figure 1a–f, respectively. The morphologies of these composites are nearly identical, resembling a thick sheet-like structure.

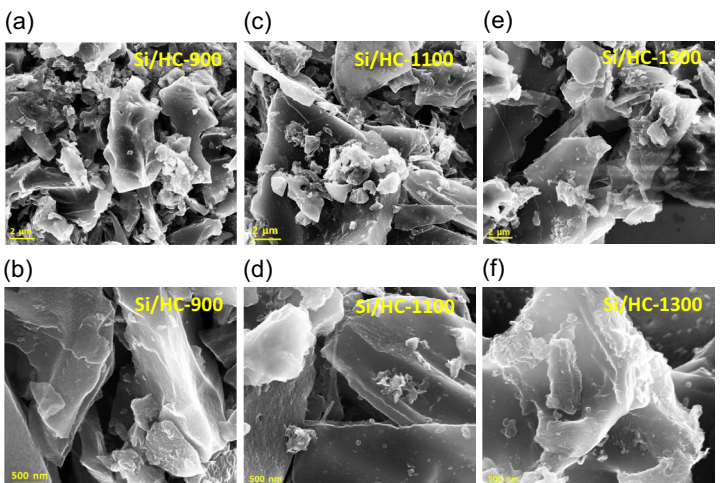
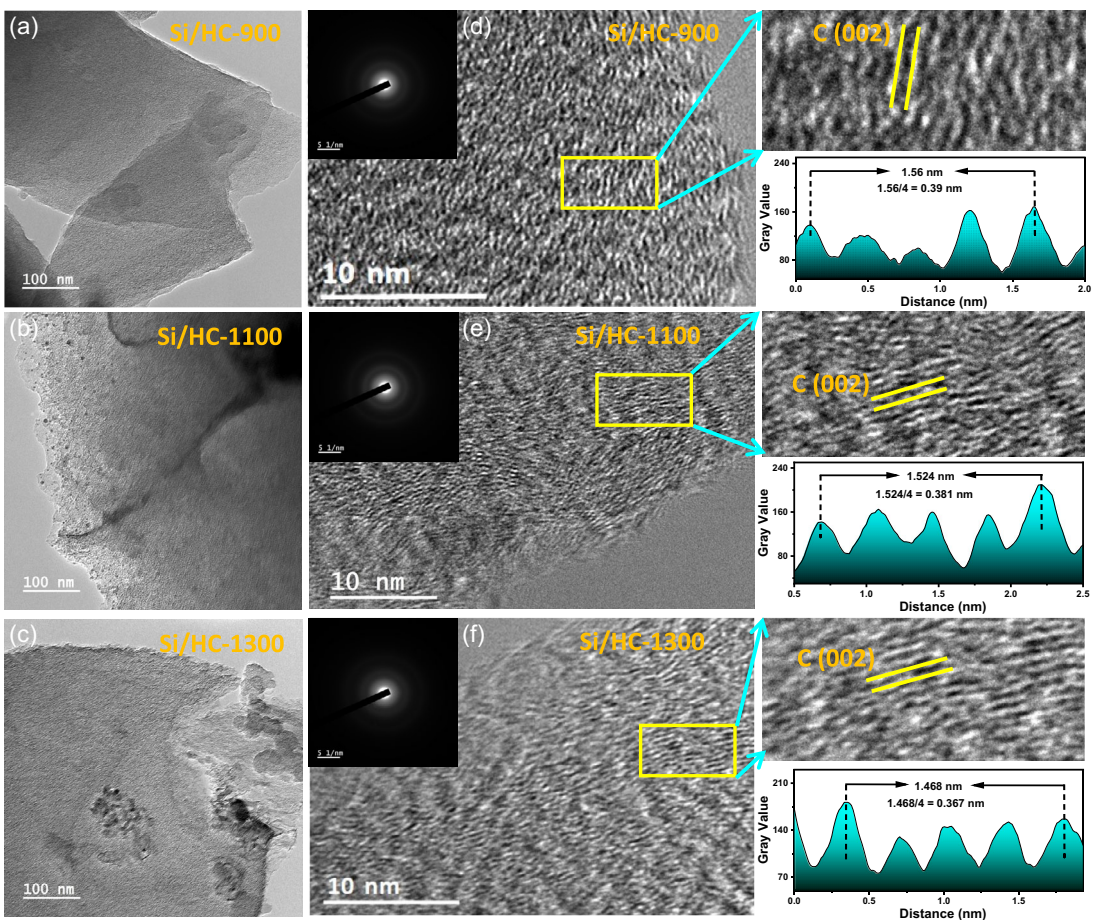


Figure 1. SEM images of the following composites: a,b) Si/HC-900; c,d) Si/HC-1100; e,f) Si/HC-1300.



**Figure 2.** a-c) TEM images of Si/HC-900, Si/HC-1100, and Si/HC-1300, respectively; d-f) HRTEM images of the composites with enlarged HRTEM images and lattice fringes, respectively (inset: SAED images).

**Figure 2** and **Figure S2, Supporting Information**, display the TEM analysis results of the composites. The TEM images of Si/HC-900, Si/HC-1100, and Si/HC-1300 are shown in Figure 2a-c and Figure S2, Supporting Information, respectively. The images further indicate that all of the composites have a thick sheet-like structure. The HRTEM images of the composites are shown in Figure 2d-f, respectively. In the HRTEM image, wrinkled carbon sheets with multilayered domains are observed. The lattice spacings for Si/HC-900, Si/HC-1100, and Si/HC-1300 are found to be  $\approx 0.39$ ,  $0.381$ , and  $0.367$  nm, respectively. The expansion of the carbon (002) plane may be due to the presence of silicone in the carbon matrix. The expanded lattice fringes promote  $\text{Na}^+$ -diffusion and storage. It was also found that the lattice spacing steadily decreases as temperature rises (Figure 2d-f). This may be due to the relatively higher degree of graphitization and presence of less amount of Si at higher temperatures. The inset of Figure 2d-f reveals the SAED images of the composites, which show very faint and defused rings, suggesting the amorphous nature of the composites.

The STEM and corresponding elemental mapping images are shown in Figure S3a-l, Supporting Information. This implies the homogeneous distribution of silicon, carbon, and oxygen across the network. The weight percentages of the composites are calculated from energy-dispersive X-ray spectroscopy, which

are tabulated in Table S1, Supporting Information. This shows that the Si/HC-1100 composite has 2.043, 1.603, and 96.354 percent of Si, O, and C content. It was also observed that the Si/C ratio falls and the O/C ratio slightly rises with increasing temperature, which may be due to the more oxidation of elements at high temperatures.

The powder X-ray diffraction (*p*-XRD) was carried out to learn more about the phase and structure of the composites. Figure S4a, Supporting Information, shows the *p*-XRD pattern of carbonized lemon leaves before and after washing. A large number of intense peaks were observed before the acid wash, which could be due to the presence of impurities such as metal salts and oxides. After acid wash, only carbon peaks remain in the *p*-XRD pattern of the carbonized leaves, which suggests the successful removal of impurities. The *p*-XRD data of Si/HC-900, Si/HC-1100, and Si/HC-1300 are displayed in Figure 3a,b. A broad peak at around  $23^\circ$  was found in all of these composites, corresponding to the C (002) plane. Figure 3a clearly shows that all of the peaks have been displaced to the left when compared to the standard graphitic peak, suggesting an extended interlayer distance of the composites. The Si inclusion in the carbon skeleton causes expansion of lattice fringes and more disorder in carbon composites. Additionally, the *p*-XRD peaks of Si/HC-X are found to progressively shift to the right as the temperature rises, indicating

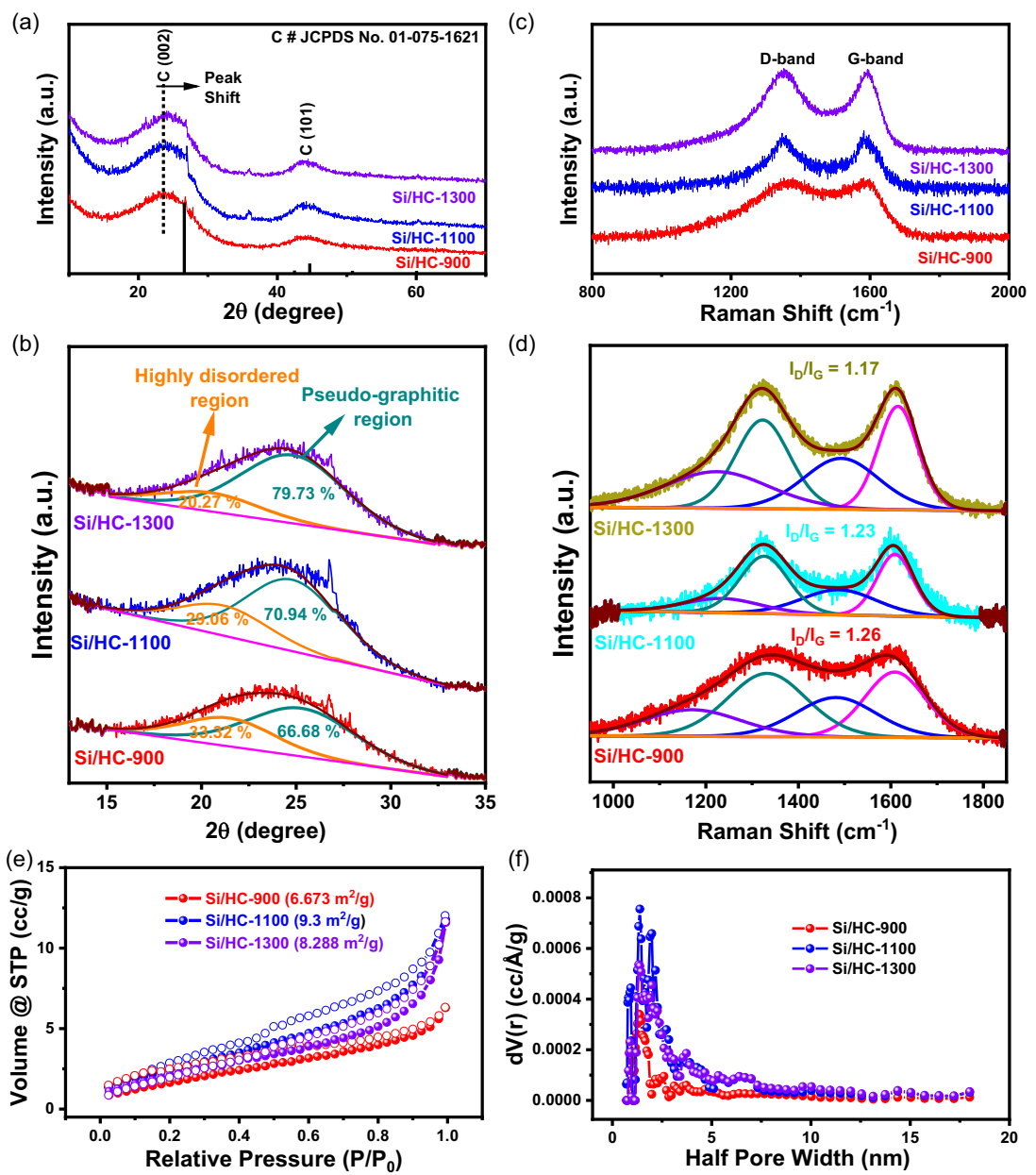


**Figure 3.** a,b)  $p$ -XRD patterns and its (002) plane fitting of Si/HC-900, Si/HC-1100, and Si/HC-1300, respectively; c,d) Raman spectra and corresponding fitted data of Si/HC-900, Si/HC-1100, and Si/HC-1300, respectively; e,f)  $N_2$  adsorption/desorption isotherm and corresponding pore size distribution plots of the composites.

increased graphitization with rising temperature. Depending on the microcrystalline phases of the HCs, three different fitting methods can be used to match the broad (002) peaks: 1) an interlayer spacing of less than 3.6 Å (graphitic domain), 2) an interlayer spacing of 3.6–4.0 Å (pseudo-graphite domain), and 3) an interlayer spacing of more than 4.0 Å (very disordered carbon).<sup>[54]</sup> The XRD patterns of all synthesized HCs display a highly disordered and pseudo-graphite carbon region, as seen in Figure 3b. In comparison to Si/HC-1300 and Si/HC-1100, respectively, the pseudo-graphite domain proportions of Si/HC-900 drop from 79.73 and 70.94 to 66.68%, but the highly disordered domain increases from 20.27 and 29.06 to 33.32 %, suggesting that the disorder degree improves with decreasing calcination temperature. Furthermore,

we computed the average thickness ( $L_c$ ) and width ( $L_a$ ) of the order-layered nanodomains using the Debye–Scherrer equation and the XRD patterns.<sup>[54]</sup>

$$L_{a/c} = K\gamma/\beta_{a/c}\cos\theta_{a/c} \quad (1)$$

The half of the diffraction angle, the X-ray wavelength, the full width at half-maximum (fwhm) of the diffraction peak, and the Scherrer constant (which is 1.84 for the (100) plane and 0.89 for the (002) plane) are represented by the variables  $\theta$ ,  $\gamma$ ,  $\beta$ , and  $K$ . The average thickness,  $L_c$ , of Si/HC-900, Si/HC-1100, and Si/HC-1300 is 1.863, 1.932, and 1.965 nm, respectively, while considering the fwhm of the (002) peak. The average width,

$L_a$  of Si/HC-900, Si/HC-1100, and Si/HC-1300 is determined by the fwhm of (100) peak, which are 9.15, 9.348, and 9.95 nm, respectively.

The pseudo-graphite domain stacking numbers,  $N$  (where  $N = L_d/d_{002} + 1$ ), were also calculated, which are 6.035, 6.22, and 6.31, corresponding to Si/HC-900, Si/HC-1100, and Si/HC-1300, respectively. The samples were also subjected to Raman examination to assess the ratio of crystalline to disordered carbon. The Raman spectra of these composites are shown in Figure 3c,d. It reveals two distinct peaks at  $\approx 1590$  and  $1350\text{ cm}^{-1}$ , respectively. These correspond to the G band (the  $E_{2g}$  symmetric vibration mode of ordered  $sp^2$  carbon sheet) and the D band (the  $A_{1g}$  symmetric vibration mode of graphene edge defects). Gaussian function fitting was used to assess the  $I_D/I_G$  integral strength ratio (Figure 3d). The smallest  $I_D/I_G$  is found to be 1.17 for Si/HC-1300, followed by 1.23 and 1.26 for Si/HC-1100 and Si/HC-900, respectively. This demonstrates that the defect concentration rises with decreasing sintering temperature. The pore size and  $N_2$  adsorption-desorption characteristics of the composites were also determined using the Brunauer–Emmett–Teller (BET) technique. The  $N_2$  adsorption/desorption isotherm and pore size distribution plots for Si/HC-900, Si/HC-1100, and Si/HC-1300 are displayed in Figure 3e,f, respectively. All the isotherms exhibit a standard IV adsorption isotherm. It was found that Si/HC-900, Si/HC-1100, and Si/HC-1300 exhibit specific surface areas of 6.673, 9.3, and  $8.288\text{ m}^2\text{ g}^{-1}$ , respectively. These areas provide channels for  $\text{Na}^+$  as well as solvent diffusion, which cause solid-electrolyte-interface (SEI) formation. It was found that all the composites possess low surface area. Therefore, low SEI formation will occur during the charge/discharge process, which increases the initial Coulombic efficiency (ICE). The pore size distribution curves of the composites show major peaks at 1.5–6 nm regions, suggesting the presence of micropores and mesopores in the composites. The micropores present in the composites only allow  $\text{Na}^+$  through (without passing any solvent), which increases the  $\text{Na}^+$  diffusion without forming SEI and, therefore, increases the  $\text{Na}^+$  storage performance.

Additionally, X-ray photoelectron spectroscopy (XPS) was used to determine the chemical state and composition of the Si/HC-1100 composite. The XPS survey scan of Si/HC-1100 is shown in Figure 4a. This again verifies the presence of Si, C, and O in the composite. The high-resolution C 1s XPS spectrum of Si/HC-1100 is displayed in Figure 4b. Five peaks, corresponding to C–Si (283.6 eV),  $sp^2$ C (284.35 eV),  $sp^3$ C (285.12 eV), C–O (286.2 eV), and O=C=O (288.1 eV), were fitted to it. Three peaks are used to fit the O 1s XPS spectrum (Figure 4c).<sup>[55,56]</sup> The C–O bond is responsible for the peak at 530.1 eV, whereas the O=C=O and Si–O bonds are responsible for the peaks at 531.9 and 533.4 eV, respectively.<sup>[57,58]</sup> The deconvoluted high-resolution XPS spectrum of Si 2p is fitted with three peaks, which are shown in Figure 4d. The peaks at 100.6 and 101.9 eV correspond to the Si–C and O–Si/Si–O–C bonds, while the peak at 103.4 eV is associated with the  $\text{SiO}_2$ .<sup>[59]</sup> All of these results confirm the existence of Si in the hard carbon skeleton.

### 3.2. Sodium-Ion Storage Performance of Si/HC-X

At first, half-cell tests were performed on the samples to determine the structural and compositional link of Si/HC-X with

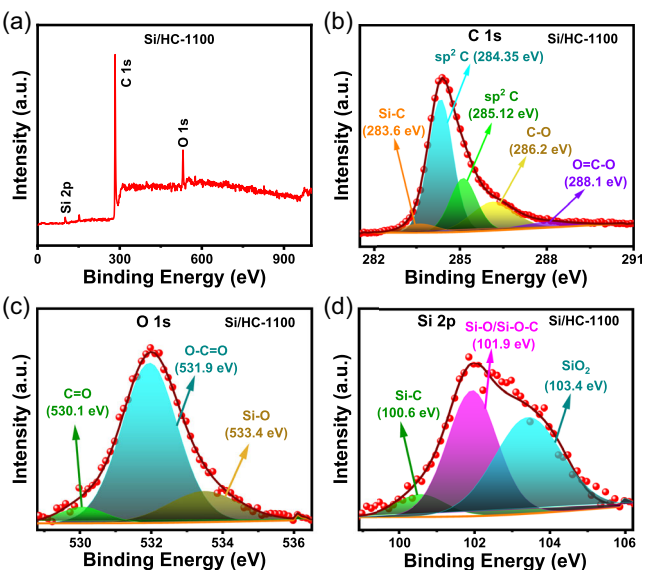
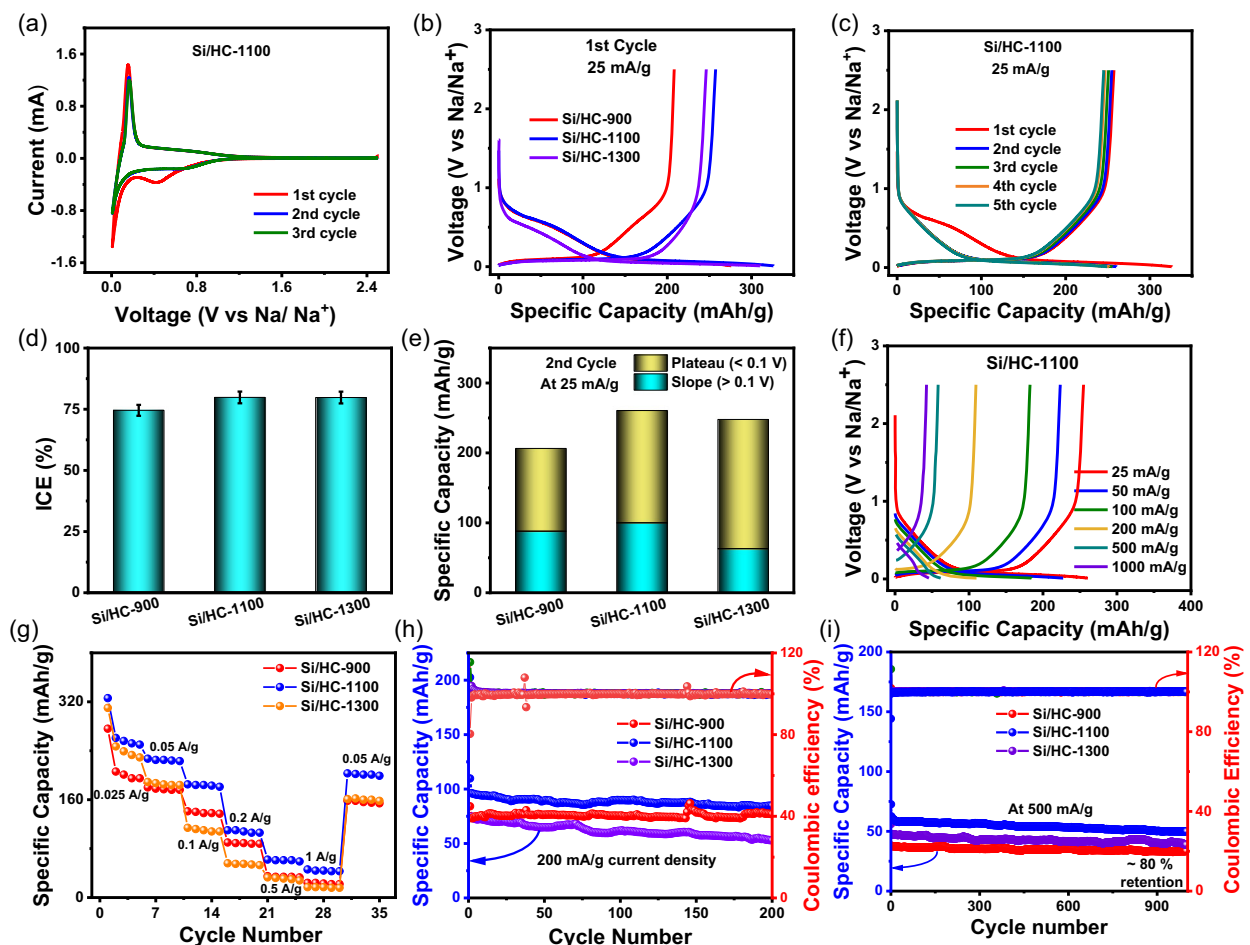


Figure 4. a) XPS survey scan of Si/HC-1100; high-resolution XPS spectra of Si/HC-1100 for b) C 1s, c) O 1s, and d) Si 2p.

electrochemical sodium ion storage characteristics. The CV curves for Si/HC-900, Si/HC-1100, and Si/HC-1300 are displayed in Figure 5a and Figure S5a,b, Supporting Information, at a scan rate of  $0.1\text{ mV s}^{-1}$  within a voltage window of  $0.01$ – $2.5\text{ V}$  (versus  $\text{Na}/\text{Na}^+$ ). In the first cycle of each composite, an obvious reduction peak was found between  $0.4$  and  $1.0\text{ V}$  (versus  $\text{Na}/\text{Na}^+$ ). This is due to the electrolyte decomposition followed by the production of solid electrolyte interphases, or SEIs.<sup>[60]</sup> Each composite thus experiences an irreversible capability loss. Additionally, there are two distinct oxidation and reduction peaks at  $\approx 0.15$  and  $0.01\text{ V}$  (versus  $\text{Na}/\text{Na}^+$ ), which is due to the insertion and extraction of sodium ions from carbon. The  $\text{Na}^+$  ion's entry into the micropores, the enlarged interlayer distances, or the formation of alloy with Si may be the cause of this. After the first cycle, the CV curves significantly overlapped, showing the high cyclability of HCs during sodiation and desodiation. Additionally, galvanostatic charge–discharge (GCD) tests were performed in the voltage range of  $0.01$  to  $2.5\text{ V}$  at a constant current of  $25\text{ mA g}^{-1}$ . Figure 5b depicts the first cycle of the charge–discharge profiles for the electrodes Si/HC-900, Si/HC-1100, and Si/HC-1300 at  $25\text{ mA g}^{-1}$  current density. Every curve can be divided into two typical regions: plateau regions ( $<0.1\text{ V}$ ) and slope regions ( $>0.1\text{ V}$ ). The electrochemical result of Si/HC-900, Si/HC-1100, and Si/HC-1300 reveals the 1st discharge capacity of  $\approx 279$ ,  $324$ , and  $310\text{ mAh g}^{-1}$ , respectively. The reversible capacity of Si/HC-1100 was found to be  $\approx 260\text{ mAh g}^{-1}$  with  $\approx 79.48\%$  initial Coulombic efficiency (Figure 5c,d). The Si/HC-1100 outperformed other composites in terms of reversible capacity, which was found to be around  $\approx 248$  and  $212\text{ mAh g}^{-1}$  for Si/HC-900 and Si/HC-1300, respectively (Figure S6a,b, Supporting Information). We also synthesized the hard carbon by extracting the metal impurities after carbonization at  $1100^\circ\text{C}$  for comparison with Si/HC-1100. The final compound was noted as Si/HC-1100-porous. It was found that Si/HC-1100 ( $9.3\text{ m}^2\text{ g}^{-1}$ ) possesses low BET surface area compared to Si/HC-1100-porous



**Figure 5.** Half cells' performances: a) CV plots of Si/HC-1100 at a scan rate of  $0.1 \text{ mV s}^{-1}$  for 3 cycles; b) first charge-discharge plots of Si/HC-900, Si/HC-1100, and Si/HC-1300 at a current density of  $25 \text{ mA g}^{-1}$ ; c) charge-discharge plots of Si/HC-1100 at a current density of  $25 \text{ mA g}^{-1}$  current densities up to 5 cycles; d) initial Coulombic efficiency plot of the composites; e) contributions of plateau and slope capacity in second cycle of the composites; f) charge-discharge plots of Si/HC-1100 at different current densities; g) rate performance of the composites; h,i) cycle stability and corresponding Coulombic efficiency of Si/HC-900, Si/HC-1100, and Si/HC-1300 at 200 and  $500 \text{ mA g}^{-1}$  current density for 200 and 1000 cycles, respectively.

( $40.3 \text{ m}^2 \text{ g}^{-1}$ ) (Figure S6c, Supporting Information). As metal impurities were present during the carbonization precursor of Si/HC-1100-porous, metallic components react vigorously with carbon framework, which makes it more porous. This causes a low ICE of Si/HC-1100-porous (52.7%) compared to Si/HC-1100 (79.8%). The charge-discharge plots and corresponding ICE of these two compounds are shown in Figure S6d,e, Supporting Information. To find the amount of capacity contributed by plateau and slope regions, a capacity contribution ratio is computed from the second discharge curve of each composite (Figure 5e). The plateau capacities of Si/HC-900, Si/HC-1100, and Si/HC-1300 are 117.9, 160.6, and  $184.9 \text{ mAh g}^{-1}$ , while the slope capacities are 88, 100, and  $63 \text{ mAh g}^{-1}$ . The adsorption of the sodium ions on the open pores and defect sites is often addressed by the slope capacity. The plateau capacity originates from the insertion of  $\text{Na}^+$  in the micropores, expanded inter-layer spacings. The plateau capacity of hard carbon anode increases with higher sintering temperature. The slope and plateau capacities will eventually need to continue maintaining high values. Adequate defects and growing interlayer spacing are present in Si/HC-1100 at a reasonable sintering temperature of 1100, which facilitates the storage

capacity at the plateau and slope areas. Figure 5f and Figure S7a,b, Supporting Information, show charge-discharge plots of Si/HC-1100, Si/HC-900, and Si/HC-1300 at different current densities, whereas Figure 5g shows the rate capabilities of these electrodes. It was found that the Si/HC-900 has average reversible capacities of 206, 180, 141, 89, 35.2, and  $24.6 \text{ mAh g}^{-1}$  at 25, 50, 100, 200, 500, and  $1000 \text{ mA g}^{-1}$  current density; in contrast, the Si/HC-1100 exhibits average reversible capacities of 261, 227, 186.9, 110, 62.1 and  $45.7 \text{ mAh g}^{-1}$ , respectively demonstrating an improvement in  $\text{Na}^+$  storage performance. Further increasing the calcination temperature, such as for Si/HC-1300, the reversible capacities decrease and show relatively poorer rate capacity, which could be due to the more graphitization of the composite at that temperature as suggested by the TEM characterization. Additionally, after returning to a current density of  $50 \text{ mA g}^{-1}$ , capacity almost sustains its value, demonstrating good reversibility and endurance in long-range charge-discharge currents. Good rate performance and capacity retention are shown by all of these composites, suggesting that sodium ions flow between wider interlayer spacings and micropores more rapidly.

The cycling performance of these composites was also evaluated for 200 cycles at 200 mAh g<sup>-1</sup> (Figure 5h). It was found that after 200 cycles, the Si/HC-1100 shows 84.6 mAh g<sup>-1</sup> specific capacities with ≈87.4% capacity retention, respectively, indicating good endurance of the composites. Furthermore, we also investigated the long-term cycling stability of all Si/HC composites for 1000 cycles at 500 mA g<sup>-1</sup> current density (Figure 5i). It displays ≈79% capacity retention of Si/HC-1100, while ≈82% and 84% retention for Si/HC-1300 and Si/HC-900 after 1000 cycles, respectively. In addition, we have also performed the cyclic stability of Si/HC-1100 at 50 mA g<sup>-1</sup> current density, which shows good cyclic stability of the material even after 100 cycles (Figure S7c, Supporting Information). An activity comparison table of Si/HC-1100 with other published carbon-based composites for SIB anodes is shown in Table S2, Supporting Information, indicating the composite's remarkable sodium ion storage and rate performance. Further, to know the effect of Si-dopant, we prepare HC-1100 by removing the Si from the precursor by HF treatment followed by calcination at 1100 °C. It is also well known that Si's alloying reaction with sodium is not favorable and is almost limited to a-Si. Generally, the crystalline Si (c-Si) is electrochemically inactive with elemental Na due to c-Si's high energy barrier of sodiation. In contrast, amorphous Si (a-Si) possesses a much lower energy barrier compared to c-Si. Si offers a capacity of

954 mAhg<sup>-1</sup> with a volume expansion of only 114% while used in SIBs in a binary phase of NaSi.<sup>[41,61]</sup> It is also found that the alloying reaction of Si with Na starts around ≈0.7 V (Na/Na<sup>+</sup>). Therefore, Si doping will directly contribute to the slope capacity. On the other hand, Si-doping also enhances the interlayer spacing, which enhances plateau capacity as well. As silicone is inherently present in the composite, it contributes to both slope and plateau capacities. Further, to know the effect of Si-doping, we prepared a hard carbon by removing Si from the composite using HF washing and named as HC-1100. It was found that the prepared compound possesses lower plateau as well as slope capacity compared to Si/HC-1100, suggesting the presence of silicone in the composite increases the plateau as well as slope capacity (Figure S7d,e, Supporting Information).

### 3.3. Sodium-Storage Mechanism

CV measurements were performed to comprehend the sodium-ion storage activity of the composites. The CV data for Si/HC-900, Si/HC-1100, and Si/HC-1300 at various scan speeds are displayed in Figure 6a and Figure S8a,b, Supporting Information, respectively. This demonstrates that the current increases as the scan rate increases. The control processes for capacitance and diffusion can be explained by the following equation

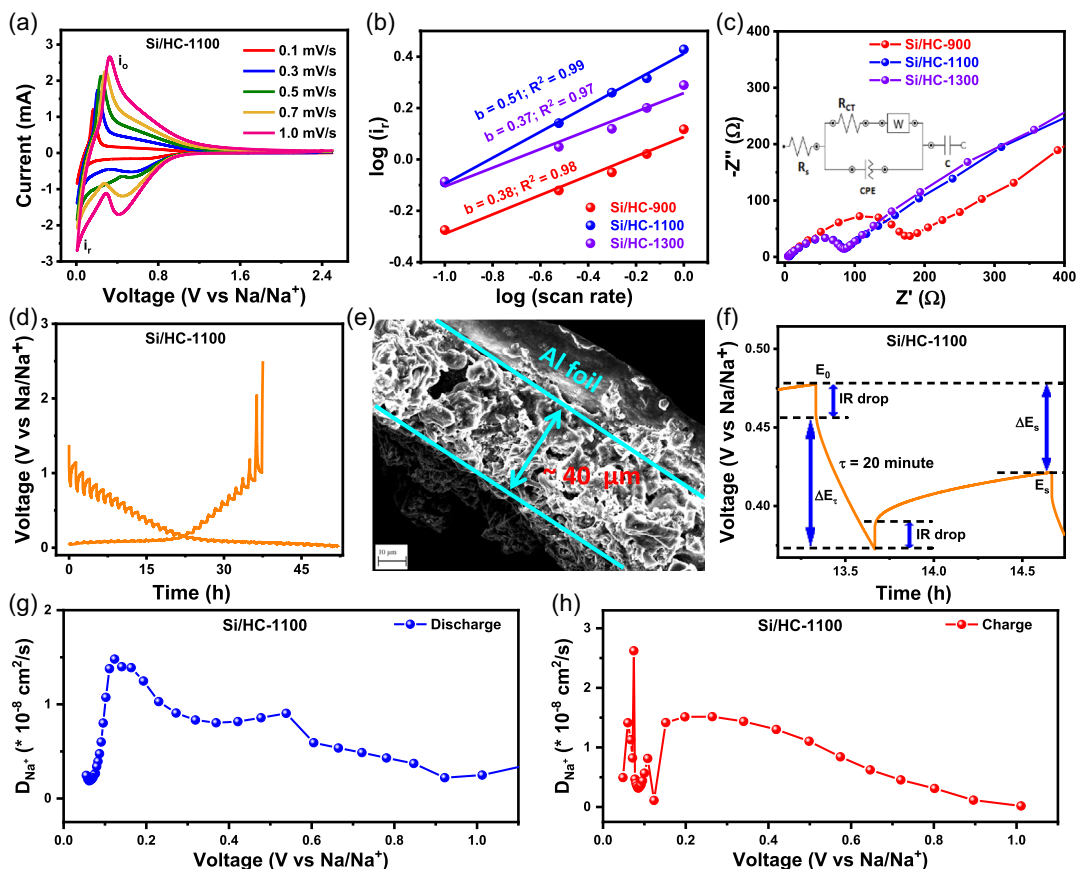


**Figure 6.** a) CV plot of Si/HC-1100 at various scan rates (0.1–1 mV s<sup>-1</sup>); b) log(*i*) and log(*v*) plots of all the composites; c) Nyquist plots of Si/HC-900, Si/HC-1100, and Si/HC-1300; d) GITT charge/discharge profiles of Si/HC-1100 at 0.01–2.5 V (versus Na/Na<sup>+</sup>); e) FESEM image of Si/HC-1100 electrode; f) potential profile with schematic labeling of various parameters before, during, and after a continuous current pulse; g,h) estimated Na<sup>+</sup> ion apparent diffusion coefficient during discharge and charge processes based on GITT charge/discharge profiles.

$$i = av^b \quad (2)$$

where  $a$  and  $b$  are the constants, and  $i$  and  $v$  represent the current response at a specific voltage and scan rate, respectively. The value of " $b$ " is between 0.5 and 1. When " $b$ " is  $\approx 0.5$ , for instance, electrolyte intercalation and deintercalation are regulated by diffusion, while surface-controlled reactions are shown when " $b$ " is  $\approx 1$ . All of these catalysts have oxidation and reduction maxima at  $\approx 0.1$  V, where a linear relationship between the  $\log(v)$  versus  $\log(i)$  curves has been found. The  $b$  value of Si/HC-1100 was found to be 0.51, which is higher than the other two composites, indicating an increasing contribution from the surface control process for Si/HC-1100 (Figure 6b). The electrochemical impedance spectroscopy (EIS) measurement was performed on the HCs in the frequency range of 100 kHz to 0.01 Hz to obtain an additional understanding of their electrochemical characteristics. All the Nyquist plots for the composites are displayed in Figure 6c. The Nyquist data of the composites was fitted with an equivalent circuit (inset: Figure 6c). At high frequencies, the Nyquist plot intercept on the  $x$ -axis can be used to compute the internal intrinsic resistance ( $R_s$ ), which includes both electrolyte resistance and contact resistance. The charge transfer resistance, constant-phase element, and Warburg diffusion resistance are denoted by the letters  $R_{CT}$ , CPE, and  $W$ , respectively. The pseudo-capacitance at the interface between the electrode material and the electrolyte is represented by the "C". The  $R_{CT}$  can be found from the semicircle. The tail of the Nyquist data at the low-frequency region is responsible for the diffusion of  $\text{Na}^+$  ions into the electrode. It was found that the Si/HC-900, Si/HC-1100, and Si/HC-1300 possess  $R_{CT}$  values of 147, 67.2, and 69.9  $\Omega$ , respectively. It was found that the  $R_{CT}$  value decreases with increasing sintering temperature. This could be due to the materials' increasing conductivity as graphitization increases with increasing temperature. The sodium-ion diffusion coefficient ( $D_{\text{Na}^+}$ ) of each of the composites can be determined using Equation (3) and (4).<sup>[62]</sup>

$$D_{\text{Na}^+}^+ = (RT)^2 / 2A^2 n^4 F^4 C^2 \sigma^2 \quad (3)$$

$$Z' = R_s + R_f + R_{CT} + \sigma\omega^{-1/2} \quad (4)$$

where  $T$ ,  $R$ ,  $n$ ,  $A$ ,  $C$ ,  $F$ ,  $\sigma$ , and  $\omega$  stand for the absolute temperature, gas constant, electron count, electrode area,  $\text{Na}^+$  concentration, Faraday constant, Warburg factor, and angular frequency. The  $\sigma$  value was computed using the  $Z'$  versus  $\omega^{-1/2}$  plot in the low-frequency domain (Figure S9a–c, Supporting Information). Among all three composites, Si/HC-1100 possesses the lowest  $\sigma$  value, suggesting its faster  $\text{Na}^+$  diffusion compared to the other composites. The impedance spectra of all the composites after cyclic test performance were also recorded, as shown in Figure S10a–c, Supporting Information. A small decrease in the semicircle was found after cycling stability, suggesting the smaller  $R_{CT}$  values of the composites, whereas  $R_s$  was nearly identical in both conditions for all the composites. The decrease in the  $R_{CT}$  value of all the composites may be due to the better wettability during the cycles. In addition, a GITT test was carried out by an electrochemical test station at room temperature to know the potential-dependent diffusion behavior of the materials.

The electrode was discharged and charged at 25 mA g<sup>-1</sup> current density for 20 min and then relaxed for 60 min to reach a steady state. The aforementioned procedure was repeatedly conducted until the potential reaches 0.01 and 2.5 V (Na/Na<sup>+</sup>) for the discharge and charge process (Figure 6d). Using the following equation and a series of assumptions and simplifications, Fick's second law of diffusion is used to determine the Na<sup>+</sup> diffusion coefficients of Si/HC-1100<sup>[63]</sup>

$$D = 4/\pi (m_B V_B / M_B S)^2 [\Delta E_S / \tau (dE_t / d\sqrt{\tau})]^2 (\tau \ll L^2 / D) \quad (5)$$

where  $m_B$  and  $M_B$  are the mass of the electrode material and molecular weight;  $L$  is the electrode thickness calculated from the SEM images, which was found to be  $\approx 40$   $\mu\text{m}$  (Figure 6e); and  $V_B$ ,  $\tau$ , and  $S$  are the molar volume of the electrode material, current duration time, and surface area of the active material estimated from BET data. Throughout the electrochemical process,  $V_B$  is assumed to be constant. It is possible to simplify Equation (1) when the variation in cell voltage and  $\tau_{1/2}$  is linear during titration<sup>[64]</sup>

$$D_{\text{Na}^+}^+ = (\Delta E_S / \Delta E_\tau)^2 * 4L^2 / \pi\tau \quad (6)$$

where  $\Delta E_\tau$  and  $\Delta E_S$  are the change of potential caused by an impulse and open-circuit potential (OCP) difference between two adjacent pulses (Figure 6f). The sodium-ion apparent diffusion coefficient (ADC) of Si/HC-1100 was found in the range of  $10^{-8}$ – $10^{-12}$  cm<sup>2</sup> s<sup>-1</sup> during the desodiation and sodiation processes (Figure 6g,h). It was found that the diffusion coefficient in this region was nearly the same. The discharge diffusion coefficient changes at 0.04 V within the voltage range of 0.01–0.10 V, suggesting distinct sodium storage mechanisms (Figure 6g). A distinct low-voltage plateau that reflects the sequential behavior of sodium ions is seen during the sodium-ion battery's discharge process. First, the ions intercalate into the pseudo-graphitic layers and then occupy the hard carbon's micropore structure.<sup>[65]</sup> Furthermore, a shift in the diffusion coefficient at 0.10 V is noted during the charging process (Figure 6h). Due to the poor interaction between the ions and the pores, sodium ions first depart the pseudo-graphitic layers between 0.01 and 0.04 V and then progressively leave the micropores between 0.04 and 0.07 V.<sup>[66,67]</sup> High diffusion coefficients of sodium ions in the plateau region (0.01–0.1 V) and the low voltage slope region (0.1–1 V) indicate sodium ions are more easily stored in the filling layer and carbon layer of the pore structure.

The electrochemical results, along with the physicochemical characterization data, indicate that the presence of Si in Si/HC-X will lead to a significant improvement in the kinetics and capacity of Na<sup>+</sup> storage, particularly in low-potential plateaus. The inherent Si dopant increases the interlayer distance of the carbon matrix, which facilitates Na<sup>+</sup> ion insertion and raises the plateau capacity. The Si also reacts with Na<sup>+</sup> and forms an alloy with it, which also contributes to the plateau capacity of the composites. Additionally, micropores formed during the calcination process also contribute to the plateau capacities of the composites by insertion of Na<sup>+</sup> into it and forming nanoclusters. The slope capacity arises from the adsorption of Na<sup>+</sup> in the defect sites and open pores for all the composites. It was found that

Si/HC-1100 exhibits higher slope capacity compared to Si/HC-900 and Si/HC-1300, which may be attributed to the greater surface area of the composite. Moving from Si/HC-900 to Si/HC-1100, the plateau capacity increases, which could be due to the greater number of micropore formations at higher temperatures. Further moving from Si/HC-1100 to Si/HC-1300, the plateau capacity increment is very low. This could be due to the significant decrease in interlayer distance, which inhibits  $\text{Na}^+$  intercalation, although micropore formation increases. This opposite phenomenon balances the plateau capacity to increase further.

The ex situ XRD and Raman were further used to examine the structural alterations of Si/HC-1100 during the  $\text{Na}^+$  storage process to validate the mechanism. The structural alterations in hard carbon materials caused by the insertion of  $\text{Na}^+$  ions are highly detectable by XRD. Figure 7a plots the ex situ XRD patterns of Si/HC-1100 acquired throughout the early desodiation and sodiation processes. The (002) peak slightly shifts to the lower angles as the Si/HC-1100 electrode sodiates, suggesting the growth of the interlayer distance. The peak returns to the higher angles once the electrode is desodiated, indicating that the interlayer distance is getting less. Prior research using in situ and ex situ XRD technologies has similarly documented comparable expansion and shrinkage of hard carbon materials during sodiation–desodiation cycles.<sup>[50,68]</sup> Regarding the sloping region, sodium “pseudo-adsorption” between highly disordered carbon with a large interlayer spacing ( $>0.40 \text{ nm}$ ) can be explained by the change in the intensity of the (002) peak of both samples during the discharge–charge process. Regarding the plateau area, the Si/HC-1100 electrode’s rich pseudo-graphitic nanodomains can intercalate plentiful  $\text{Na}^+$  into the graphitic-like layers, causing the spacing to expand and the peak intensity to drop. Consequently, it can

be said that  $\text{Na}^+$  intercalation dominates the sodiation process of Si/HC-1100 material in the low-voltage plateau area.

Raman spectroscopy can provide further information to XRD findings. The storage of  $\text{Na}^+$  in the Si/HC-1100 sample was examined using ex situ Raman spectroscopy (Figure 7b). When electrons move to graphitic layers and alkali metal ions are inserted, the  $\pi^*$  antibonding band is often occupied, which weakens and lengthens the C–C bond and causes the G-band to redshift.<sup>[69]</sup> Moreover, the breathing vibration of  $\text{sp}^2$  carbon rings near the defect and the edge of the carbon layer is often restricted by the adsorption of alkali metal ions at defective sites and pores, which weakens the D-band.<sup>[70,71]</sup> Figure 7c plots the G-band position variation and the  $I_D/I_G$  ratios with discharge capacity for the Si/HC-1100 electrode, respectively. As the sloped region is sodiated, the adsorption of  $\text{Na}^+$  between bigger carbon layers ( $>0.40 \text{ nm}$ ) causes the G-band peak to gradually redshift from OCP ( $1595 \text{ cm}^{-1}$ ) to 0.1 V ( $1574 \text{ cm}^{-1}$ ). The G-band peak is clearly widened and redshifted to  $1560 \text{ cm}^{-1}$  at 0.01 V during the subsequent discharge process in the voltage plateau area (Figure 7c). Intercalation of  $\text{Na}^+$  between graphitic-like layers is responsible for the redshift and broadening of the G-band peak for the sodiated Si/HC-1100 electrode (Figure 7c).

The D-band location did not change as sodiation went on, but the  $I_D/I_G$  ratios dropped from 1.24 at OCP to 1.14 at 0.1 V, indicating that  $\text{Na}^+$  ions were adsorbed at the defect sites. The ratios of  $I_D/I_G$  also progressively dropped to 1.1 at 0.002 V in the voltage plateau region, which is indicative of either the pore filling of Na clusters or the adsorption of  $\text{Na}^+$  ions at the pore surface. The adsorption or filling of  $\text{Na}^+$  ions in the pores is not significant because of the subtle decline in  $I_D/I_G$  in the voltage plateau area. The Raman data show that the material can undergo both

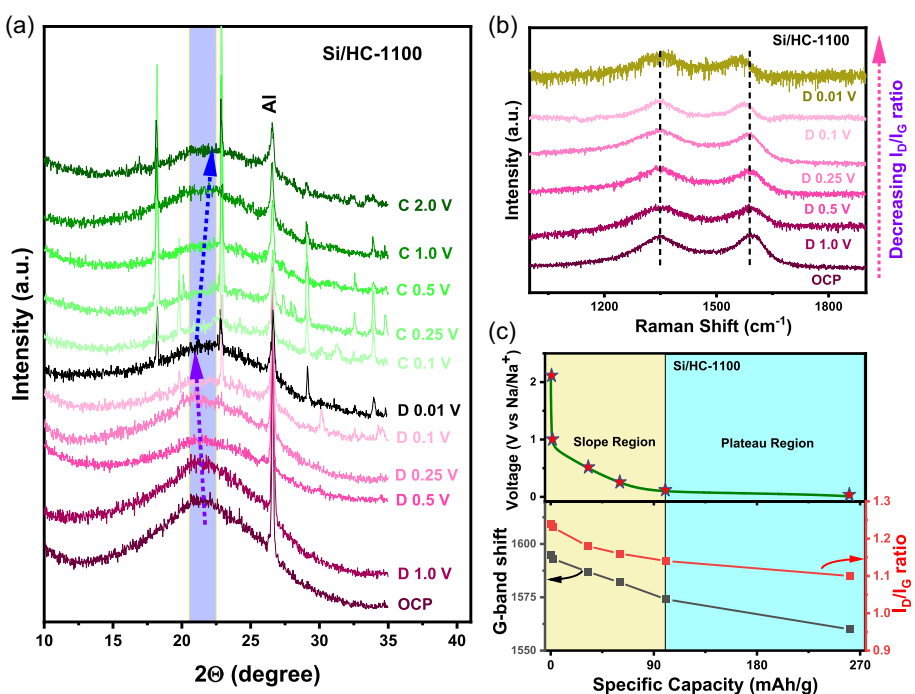
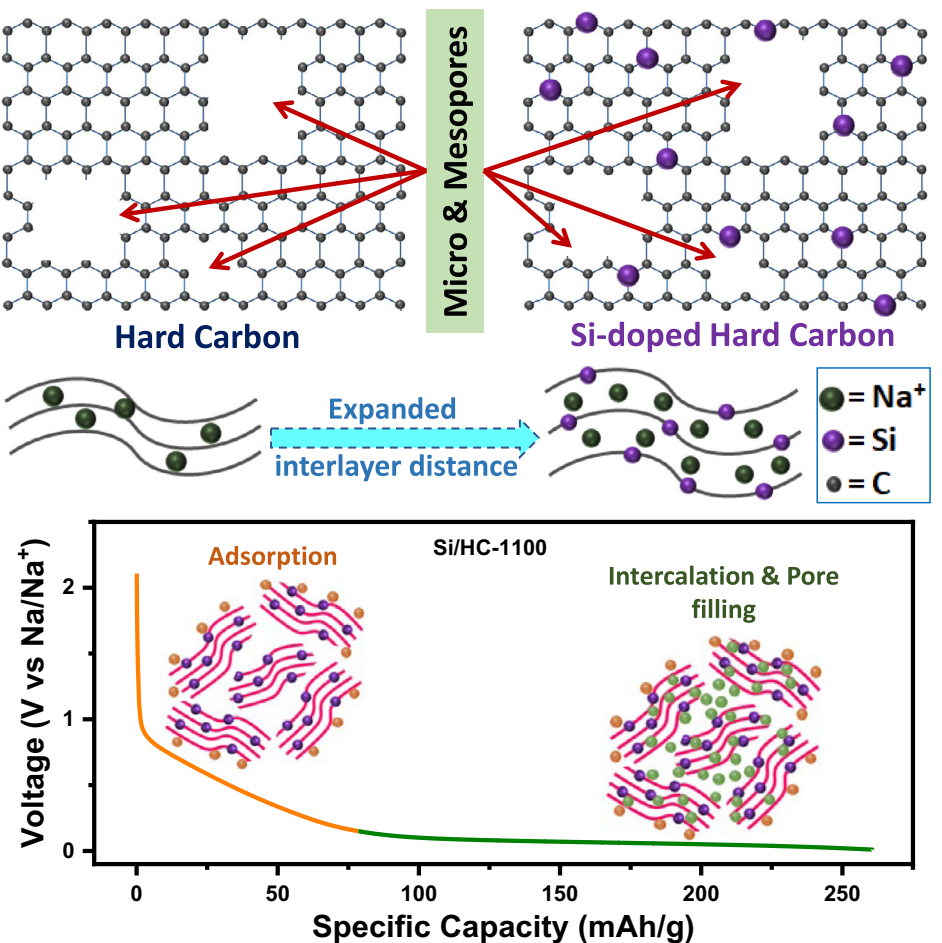


**Figure 7.** a) Ex situ XRD measurement of Si/HC-1100 during different sodiation and desodiation potential; b,c) Ex situ Raman measurement and corresponding G-band shift &  $I_D/I_G$  ratio change of Si/HC-1100 during sodiation.



Scheme 2. Schematic diagram for Na<sup>+</sup> storage mechanism with the microstructure of the hard carbon.

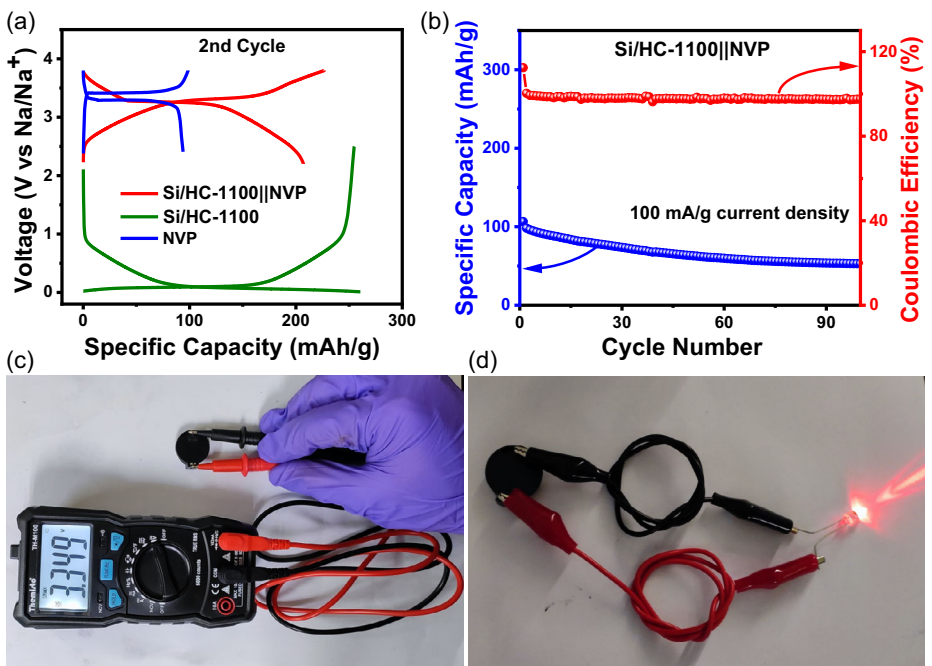


Figure 8. Full cell performance of Si/HC-1100 || NVP system: a) Charge–discharge curves at 25 mA g<sup>-1</sup> current density; b) cycle stability at 100 mA g<sup>-1</sup> current density; c,d) digital image of the cell showing OCP and lightening of LED light.

pore-filling and interlayer intercalation; interlayer intercalation mostly contributes to Si/HC-1100's capacity to store  $\text{Na}^+$ . Scheme 2 depicts a schematic illustration of a sodium ion storage mechanism with Si doping and microstructure of the composites.

### 3.4. Full Cell Performance

The practical applicability of Si/HC-1100 was also investigated by constructing a full cell with NVP ( $\text{Na}_3\text{V}(\text{PO}_4)_3$ ) as the cathode and Si/HC-1100 as the anode with 1.0 M  $\text{NaPF}_6$  in an EC:DEC:DMC (2:1:1) electrolyte. The loading of cathode active material was adjusted by the capacity of anode material. Figure 8a displays a high discharge capacity of  $\approx 94$  and  $261 \text{ mAh g}^{-1}$  of the cathode (NVP) and anode (Si/HC-1100) at  $25 \text{ mA g}^{-1}$  current density of the half cells. The full cell (NVP || Si/HC-1100) displays a capacity of  $\approx 207 \text{ mAh g}^{-1}$  at  $25 \text{ mA g}^{-1}$  current density depending on the active mass of the anode side, which is close to the capacity of the half-cell, suggesting the high usability of the materials in the full-cell. The system was also tested for cyclic stability, which demonstrates good capacity retention even after 100 cycles (Figure 8b). For practical usability, we have tried to lighten a 3 V LED light using the full cell. Before lightening, the cell was charged up to 3.8 V ( $\text{Na}/\text{Na}^+$ ). Then, the cell was allowed to stand for 4 h. OCP was then measured by a multimeter.

The OCP of the cell was found to be  $\approx 3.349 \text{ V}$  ( $\text{Na}/\text{Na}^+$ ), which was then connected with the LED light, as shown in the inset of Figure 8c,d. It was found that the cell was able to lighten the LED light. All these experimental data suggest that Si/HC-1100 has great potential to be used as anode material in SIBs.

## 4. Conclusions

To summarize, *Citrus limon* leaf-derived silicon hard carbon composites (Si/HC-X) were prepared by simple thermal treatment in the presence of an Ar atmosphere for SIB anode materials. The microstructure and Si-containing groups of the composites are mapped using XRD, XPS, TEM, BET, and Raman studies. The Si content and microstructure have a correlation with the  $\text{Na}^+$  ion storage performance of the composites. With increasing carbonization temperatures, micro- and nanopore formation increases while interlayer spacing decreases, which balances the  $\text{Na}^+$  storage performance. Therefore, an optimum temperature is necessary. All the composites show good capacity and rate performance due to the large interlayer spacing, Si-dopant, and presence of micro- or nanopores. The optimized Si/HC-1100 composite shows a maximum specific reversible capacity of  $\approx 261 \text{ mAh g}^{-1}$  at  $25 \text{ mA g}^{-1}$  current density with good cycling stability, maintaining  $\approx 87.4\%$  of its capacity after 200 cycles at a current density of  $200 \text{ mA g}^{-1}$ . The GITT study suggests fast  $\text{Na}^+$  diffusion kinetics of Si/HC-1100, which could be due to the easy insertion of  $\text{Na}^+$  in the expanded interlayers and micro-pores. The ex situ XRD and Raman analysis further shows that  $\text{Na}^+$  stores in Si/HC-1100 through "adsorption-intercalation-pore filling" mechanism. Moreover, the full-cell (Si/HC-1100 || NVP) demonstrated good cycling stability and a reversible capacity

of  $\approx 207 \text{ mAh g}^{-1}$  from the anode side at  $25 \text{ mA g}^{-1}$  current, indicating that the composite has a great potential to be used in SIBs. This research may offer insight into synthesizing biomass-derived silicon-doped carbonaceous materials for effective energy storage devices.

## Acknowledgements

The authors are thankful to the Department of Atomic Energy (DAE), India, for financial support (grants No - RIN 4002). The authors also thank NISER for the infrastructure. The authors are also thankful to the Centre for Interdisciplinary Science (CIS) for SEM and TEM analysis.

## Conflict of Interest

The authors declare no conflict of interest

## Data Availability Statement

The data that support the findings of this study are available in the supplementary material of this article.

**Keywords:** anodes · *Citrus limon* · full cells · hard carbon · silicon · sodium-ion batteries

- [1] A. Manthiram, *ACS Cent. Sci.* **2017**, *3*, 1063.
- [2] J.-M. Tarascon, *Nat. Chem.* **2010**, *2*, 510.
- [3] S. Y. Hong, Y. Kim, Y. Park, A. Choi, N.-S. Choi, K. T. Lee, *Energy Environ. Sci.* **2013**, *6*, 2067.
- [4] D. Kundu, E. Talaie, V. Duffort, L. F. Nazar, *Angew. Chem. Int. Ed.* **2015**, *54*, 3431.
- [5] Y. Zhang, M. Wu, J. Ma, G. Wei, Y. Ling, R. Zhang, Y. Huang, *ACS Cent. Sci.* **2020**, *6*, 232.
- [6] C. Wang, L. Liu, S. Zhao, Y. Liu, Y. Yang, H. Yu, S. Lee, G.-H. Lee, Y.-M. Kang, R. Liu, F. Li, J. Chen, *Nat. Commun.* **2021**, *12*, 2256.
- [7] Q. Ni, Y. Bai, F. Wu, C. Wu, *Adv. Sci.* **2017**, *4*, 1600275.
- [8] M. Bianchini, P. Xiao, Y. Wang, G. Ceder, *Adv. Energy Mater.* **2017**, *7*, 1700514.
- [9] W. Wang, Y. Gang, Z. Hu, Z. Yan, W. Li, Y. Li, Q.-F. Gu, Z. Wang, S.-L. Chou, H.-K. Liu, S.-X. Dou, *Nat. Commun.* **2020**, *11*, 980.
- [10] W. Wang, Y. Gang, J. Peng, Z. Hu, Z. Yan, W. Lai, Y. Zhu, D. Appadoo, M. Ye, Y. Cao, Q.-F. Gu, H.-K. Liu, S.-X. Dou, S.-L. Chou, *Adv. Funct. Mater.* **2022**, *32*, 2111727.
- [11] Y. Tang, J. He, J. Peng, J. Yang, Z. Wu, P. Liu, K. Zhou, S. Hu, L. Hu, X. Wang, *Energy Fuels* **2024**, *38*, 7389.
- [12] Y. Zhang, X. Li, P. Dong, G. Wu, J. Xiao, X. Zeng, Y. Zhang, X. Sun, *ACS Appl. Mater. Interfaces* **2018**, *10*, 42796.
- [13] M. D. Slater, D. Kim, E. Lee, C. S. Johnson, *Adv. Funct. Mater.* **2013**, *23*, 947.
- [14] Y.-B. Niu, Y.-X. Yin, Y.-G. Guo, *Small* **2019**, *15*, 1900233.
- [15] D. Wu, C. Zhu, M. Wu, H. Wang, J. Huang, D. Tang, J. Ma, *Angew. Chem. Int. Ed.* **2022**, *61*, e202214198.
- [16] K. Chayambuka, G. Mulder, D. L. Danilov, P. H. L. Notten, *Adv. Energy Mater.* **2018**, *8*, 1800079.
- [17] H. Wang, C. Zhu, J. Liu, S. Qi, M. Wu, J. Huang, D. Wu, J. Ma, *Angew. Chem. Int. Ed.* **2022**, *61*, e202208506.
- [18] L.-F. Zhao, Z. Hu, W.-H. Lai, Y. Tao, J. Peng, Z.-C. Miao, Y.-X. Wang, S.-L. Chou, H.-K. Liu, S.-X. Dou, *Adv. Energy Mater.* **2021**, *11*, 2002704.
- [19] X. Chen, X. Feng, B. Ren, L. Jiang, H. Shu, X. Yang, Z. Chen, X. Sun, E. Liu, P. Gao, *Nano-Micro Lett.* **2021**, *13*, 71.
- [20] H. Hou, X. Qiu, W. Wei, Y. Zhang, X. Ji, *Adv. Energy Mater.* **2017**, *7*, 1602898.
- [21] M. Zhang, Y. Li, F. Wu, Y. Bai, C. Wu, *Nano Energy* **2021**, *82*, 105738.

- [22] Y. S. Yun, K.-Y. Park, B. Lee, S. Y. Cho, Y.-U. Park, S. J. Hong, B. H. Kim, H. Gwon, H. Kim, S. Lee, Y. W. Park, H.-J. Jin, K. Kang, *Adv. Mater.* **2015**, *27*, 6914.
- [23] Y. Qi, Y. Lu, F. Ding, Q. Zhang, H. Li, X. Huang, L. Chen, Y.-S. Hu, *Angew. Chem. Int. Ed.* **2019**, *58*, 4361.
- [24] V. Cardoso, J. L. A. Brás, I. F. Costa, L. M. A. Ferreira, L. T. Gama, R. Vincentelli, B. Henrissat, C. M. G. A. Fontes, *Int. J. Mol. Sci.* **2022**, *23*, 4024.
- [25] L. Li, M. Sun, Z. Xu, Z. Wang, K. Liu, Y. Chen, Z. Wang, H. Chen, H. Yang, *Coll. Surf. A: Physicochem. Eng. Aspects* **2023**, *661*, 130927.
- [26] H. Guo, K. Sun, Y. Lu, H. Wang, X. Ma, Z. Li, Y.-S. Hu, D. Chen, *Chin. Phys. B* **2019**, *28*, 068203.
- [27] J. Xiang, W. Lv, C. Mu, J. Zhao, B. Wang, *J. Alloys Compd.* **2017**, *701*, 870.
- [28] F. Zhang, Y. Yao, J. Wan, D. Henderson, X. Zhang, L. Hu, *ACS Appl. Mater. Interfaces* **2017**, *9*, 391.
- [29] A. A. Arie, B. Tekin, E. Demir, R. Demir-Cakan, *Mater. Technol.* **2019**, *34*, 515.
- [30] L. Cao, W. Hui, Z. Xu, J. Huang, P. Zheng, J. Li, Q. Sun, *J. Alloys Compd.* **2017**, *695*, 632.
- [31] W. Lv, F. Wen, J. Xiang, J. Zhao, L. Li, L. Wang, Z. Liu, Y. Tian, *Electrochim. Acta* **2015**, *176*, 533.
- [32] E. M. Lotfabad, J. Ding, K. Cui, A. Kohandehghan, W. P. Kalisvaart, M. Hazelton, D. Mitlin, *ACS Nano* **2014**, *8*, 7115.
- [33] M. Dahbi, M. Kiso, K. Kubota, T. Horiba, T. Chafik, K. Hida, T. Matsuyama, S. Komaba, *J. Mater. Chem. A* **2017**, *5*, 9917.
- [34] T. Zhang, J. Mao, X. Liu, M. Xuan, K. Bi, X. L. Zhang, J. Hu, J. Fan, S. Chen, G. Shao, *RSC Adv.* **2017**, *7*, 41504.
- [35] K.-I. Hong, L. Qie, R. Zeng, Z.-q. Yi, W. Zhang, D. Wang, W. Yin, C. Wu, Q. J. Fan, W. X. Zhang, Y. H. Huang, *J. Mater. Chem. A* **2014**, *2*, 12733.
- [36] K. Kim, D. G. Lim, C. W. Han, S. Osswald, V. Ortalan, J. P. Youngblood, V. G. Pol, *ACS Sustain. Chem. Eng.* **2017**, *5*, 8720.
- [37] M. K. Rybarczyk, Y. Li, M. Qiao, Y.-S. Hu, M.-M. Titirici, M. Lieder, *J. Energy Chem.* **2019**, *29*, 17.
- [38] H. Darjazi, L. Bottoni, H. R. Moazami, S. J. Rezvani, L. Balducci, L. Sbrascini, A. Staffolani, A. Tombesi, F. Nobili, *Mater. Today Sustain.* **2023**, *21*, 100313.
- [39] A. M. G. N. Mamede, C. C. d. S. Coelho, O. Freitas-Silva, H. T. G. Barboza, A. G. Soares, *Nutritional Composition And Antioxidant Properties Of Fruits And Vegetables*, A.K. JaiswalAcademic Press **2020**, pp. 377–392.
- [40] Y.-C. Zhang, Y. You, S. Xin, Y.-X. Yin, J. Zhang, P. Wang, X.-s. Zheng, F.-F. Cao, Y.-G. Guo, *Nano Energy* **2016**, *25*, 120.
- [41] S. C. Jung, D. S. Jung, J. W. Choi, Y.-K. Han, *J. Phys. Chem. Lett.* **2014**, *5*, 1283.
- [42] X. Wang, Q. Hu, J. Cui, J. Hou, Y. Huang, X. Liu, *ACS Appl. Mater. Interfaces* **2025**, *17*, 12004.
- [43] D. A. Stevens, J. R. Dahn, *J. Electrochem. Soc.* **2001**, *148*, A803.
- [44] D. A. Stevens, J. R. Dahn, *J. Electrochem. Soc.* **2000**, *147*, 4428.
- [45] B. Zhang, C. M. Ghimbeu, C. Laberty, C. Vix-Guterl, J.-M. Tarascon, *Adv. Energy Mater.* **2016**, *6*, 1501588.
- [46] P. Bai, Y. He, X. Zou, X. Zhao, P. Xiong, Y. Xu, *Adv. Energy Mater.* **2018**, *8*, 1703217.
- [47] X. Zhang, Y. Cao, G. Li, G. Liu, X. Dong, Y. Wang, X. Jiang, X. Zhang, Y. Xia, *Small* **2024**, *20*, 2311197.
- [48] S. Qiu, L. Xiao, M. L. Sushko, K. S. Han, Y. Shao, M. Yan, X. Liang, L. Mai, J. Feng, Y. Cao, X. Ai, H. Yang, J. Liu, *Adv. Energy Mater.* **2017**, *7*, 1700403.
- [49] N. Sun, Z. Guan, Y. Liu, Y. Cao, Q. Zhu, H. Liu, Z. Wang, P. Zhang, B. Xu, *Adv. Energy Mater.* **2019**, *9*, 1901351.
- [50] C. Bommier, T. W. Surta, M. Dolgos, X. Ji, *Nano Lett.* **2015**, *15*, 5888.
- [51] M. Song, Z. Yi, R. Xu, J. Chen, J. Cheng, Z. Wang, Q. Liu, Q. Guo, L. Xie, C. Chen, *Energy Storage Mater.* **2022**, *51*, 620.
- [52] Z. Zheng, S. Hu, W. Yin, J. Peng, R. Wang, J. Jin, B. He, Y. Gong, H. Wang, H. J. Fan, *Adv. Energy Mater.* **2024**, *14*, 2303064.
- [53] J. Zhao, X.-X. He, W.-H. Lai, Z. Yang, X.-H. Liu, L. Li, Y. Qiao, Y. Xiao, L. Li, X. Wu, S.-L. Chou, *Adv. Energy Mater.* **2023**, *13*, 2300444.
- [54] R. Samanta, S. Roy, S. Barman, *Energy Fuels* **2024**, *38*, 19867.
- [55] C. L. Chiang, J. M. Yang, *Novel Fire Retard. Polymers Comp. Mater.* **2017**, *295*, <https://doi.org/10.1016/B978-0-08-100136-3-00011-X>.
- [56] M. Y. Bashouti, Y. Paska, S. R. Puniredd, T. Stelzner, S. Christiansen, H. Haick, *Phys. Chem. Chem. Phys.* **2009**, *11*, 3845.
- [57] J. W. Ma, W. J. Lee, J. M. Bae, K. S. Jeong, S. H. Oh, J. H. Kim, S. H. Kim, J. H. Seo, J. P. Ahn, H. Kim, M. H. Cho, *Nano Lett.* **2015**, *15*, 7204.
- [58] Y. C. G. Kwan, G. M. Ng, C. H. A. Huan, *Thin Solid Films* **2015**, *590*, 40.
- [59] A. Kaur, P. Chahal, T. Hogan, *IEEE Electron Device Lett.* **2016**, *37*, 142.
- [60] P. Liu, Y. Li, Y.-S. Hu, H. Li, L. Chen, X. Huang, *J. Mater. Chem. A* **2016**, *4*, 13046.
- [61] S.-M. Zheng, Y.-R. Tian, Y.-X. Liu, S. Wang, C.-Q. Hu, B. Wang, K.-M. Wang, *Rare Metals* **2021**, *40*, 272.
- [62] M. Sun, Y. Qu, F. Zeng, Y. Yang, K. Xu, C. Yuan, Z.-H. Lu, *Ind. Eng. Chem. Res.* **2022**, *61*, 2126.
- [63] W. Weppner, R. A. Huggins, *J. Electrochem. Soc.* **1977**, *124*, 1569.
- [64] Y. Xi, X. Wang, H. Wang, M. Wang, G. Wang, J. Peng, N. Hou, X. Huang, Y. Cao, Z. Yang, D. Liu, X. Pu, G. Cao, R. Duan, W. Li, J. Wang, K. Zhang, K. Xu, J. Zhang, X. Li, *Adv. Funct. Mater.* **2024**, *34*, 2309701.
- [65] Y. He, X. Han, Y. Du, B. Song, B. Zhang, W. Zhang, P. Xu, *Nano Res.* **2018**, *11*, 2573.
- [66] Z. Zhang, G. Li, G. Liang, P. Zhao, X. Gong, J. Dai, H. Xiong, Z. Zhang, J. Mao, S. Zhang, B. Wang, *Batteries Supercaps* **2024**, *7*, e202300552.
- [67] H. Chen, N. Sun, Q. Zhu, R. A. Soomro, B. Xu, *Adv. Sci.* **2022**, *9*, 2200023.
- [68] J. Ding, H. Wang, Z. Li, A. Kohandehghan, K. Cui, Z. Xu, B. Zahiri, X. Tan, E. M. Lotfabad, B. C. Olsen, D. Mitlin, *ACS Nano* **2013**, *7*, 11004.
- [69] S. Komaba, W. Murata, T. Ishikawa, N. Yabuuchi, T. Ozeki, T. Nakayama, A. Ogata, K. Gotoh, K. Fujiwara, *Adv. Funct. Mater.* **2011**, *21*, 3859.
- [70] X. Zhong, Y. Li, L. Zhang, J. Tang, X. Li, C. Liu, M. Shao, Z. Lu, H. Pan, B. Xu, *ACS Appl. Mater. Interfaces* **2019**, *11*, 2970.
- [71] S. Huang, Z. Li, B. Wang, J. Zhang, Z. Peng, R. Qi, J. Wang, Y. Zhao, *Adv. Funct. Mater.* **2018**, *28*, 1706294.

Manuscript received: May 30, 2025

Revised manuscript received: June 26, 2025

Version of record online: